



This is a repository copy of *ISPH wave simulation by using an internal wave maker*.

White Rose Research Online URL for this paper:
<http://eprints.whiterose.ac.uk/86311/>

Version: Accepted Version

Article:

Liu, X., Lin, P. and Shao, S. (2014) ISPH wave simulation by using an internal wave maker. *Coastal Engineering*, 95. 160 - 170. ISSN 0378-3839

<https://doi.org/10.1016/j.coastaleng.2014.10.007>

Reuse

Unless indicated otherwise, fulltext items are protected by copyright with all rights reserved. The copyright exception in section 29 of the Copyright, Designs and Patents Act 1988 allows the making of a single copy solely for the purpose of non-commercial research or private study within the limits of fair dealing. The publisher or other rights-holder may allow further reproduction and re-use of this version - refer to the White Rose Research Online record for this item. Where records identify the publisher as the copyright holder, users can verify any specific terms of use on the publisher's website.

Takedown

If you consider content in White Rose Research Online to be in breach of UK law, please notify us by emailing eprints@whiterose.ac.uk including the URL of the record and the reason for the withdrawal request.



eprints@whiterose.ac.uk
<https://eprints.whiterose.ac.uk/>

ISPH Wave Simulation by Using an Internal Wave Maker

Xin Liu^a, Pengzhi Lin^{a,*}, Songdong Shao^b

^a State Key Laboratory of Hydraulics and Mountain River Engineering, Sichuan University, Chengdu, 610065, China.

^b Department of Civil and Structural Engineering, University of Sheffield, Mappin Street, Sheffield, S1 3JD, United Kingdom. (College of Hydraulic and Hydroelectric Engineering, Qinghai University, Xining, 810016, China)

Abstract

In this paper, a non-reflection internal wave maker algorithm is included in the incompressible Smoothed Particle Hydrodynamics (ISPH) model for the wave simulations. A momentum source term derived from the Boussinesq equations is employed and added into the Lagrangian form of Navier-Stokes equations for the wave generations that are not affected by the reflected waves. In this work, the technical details of implementing the internal force into the ISPH equations are proposed and a series of numerical tests are carried out for the selection of relevant parameters and investigation of their sensitivities in different wave conditions. In model applications, the problems of wave propagation and reflection from a vertical wall are studied to verify the model performance in standing wave generations and the non-reflection characteristics of the internal wave maker. Furthermore, a more challenging wave decomposition process over a trap-

* Corresponding author, Tel.: +86 028-85406172; Fax: +86 028-85405148

E-mail address: cvelinpz@126.com

ezoid breakwater is presented, which has not been fully investigated by other similar particle-based methods. The simulation results of wave surface profile on six wave gauges agree well with the experimental results and this shows that the present model with the non-reflection internal wave maker can provide a more robust particle modeling tool for the long time simulation of wave and wave-structure interactions.

Key words: ISPH, internal wave maker, non reflection, momentum source term, wave simulation, long time.

1. Introduction

In the wave generations in Smoothed Particle Hydrodynamics (SPH) method, the pioneering work was attributed to Monaghan (1994) in which the initial wave parameters based on the theoretical solutions were given to fluid particles to generate the target wave. However, this method can only be used to generate one wave event, such as the solitary wave, because the resetting of the initial wave parameters is not possible for a series of wave event. Another more widely used wave generation algorithm employs the numerical wave paddle to push the water in different frequencies and amplitudes and can generate any kinds of the wave found in the practical field. The earliest work to use the wave paddle for a mesh free particle modeling approach could be traced back to Monaghan (1994). The wave paddle was also used by Gotoh and Sakai (1999), who studied the cnoidal wave breaking on a slope using the Moving Particle Semi-implicit (MPS) method (Koshizuka et al., 1998). Later studies have extended this popular wave making concept to the periodic waves (Khayyer and Gotoh, 2009), solitary waves (Dao et al., 2013) and random waves (Zheng et al., 2010). In these models, a common practice was that the moving solid wall was used to simulate the wave paddle and the wave

maker theory was applied in the same way as that used in the laboratory experiment. In this sense, the SPH wave paddle can generate a variety of the laboratory waves without any theoretical barrier. Besides, numerical water waves can also be generated by other similar approaches, such as a moving structure ([Gallati et al., 2005](#)) and landslide falling object ([Du et al., 2006](#)).

By using the above wave paddle method, however, for the long-time wave-structure interaction problems, the reflected waves from the structure will propagate towards the numerical wave maker and then be reflected. The secondary reflection wave could strongly affect the subsequent wave propagations and result in the distortions of wave height. This has put a severe limitation on the particle-based methods to achieve long-time wave simulations, which is indispensable in order to get the required wave dynamics. One temporary remedy would be to employ a large computational domain to delay the arrival of the secondary reflection wave at expensive CPU cost. On the other hand, the damping layer concept can also be used to absorb the undesirable reflection waves. However, this can also increase the size of computational domain, and the efficiency of numerical damping layers could differ quite a lot under different wave conditions and layer coefficients ([Molteni et al., 2013](#)). By realizing the above issues, a self-absorbing wave paddle concept was initially presented for the separation of incident and reflected waves by [Frigaard and Brorsen \(1995\)](#), although this method involved complex wave theories and relied on the accuracy of water surface measurements in front of the wave paddle. Following this, [Hayashi et al. \(2000\)](#) developed a practical non-reflection wave paddle to study the wave breaking and overtopping of an upright seawall using the MPS method. [Shibata et al. \(2011\)](#) proposed a transparent boundary condition to generate the incident waves and absorb the reflected waves in a much more

efficient manner. Didier and Neves (2012) developed a piston-type wave maker with the dynamic wave absorption functions which enabled the outgoing waves to be absorbed. The most recent work was attributed to Skillen et al. (2013) who used a paddle-free Fourier series analysis to assign the particles with relevant wave kinematics and they computed a large-scale SPH wave propagation problem.

Although quite a few good progresses have been made in the wave generations using the above non-reflection wave paddles, alternative approaches should be explored to find a more efficient wave generation mechanism in SPH so as to fully demonstrate its potentials in the wave simulation. In this regard, some previous studies in the grid-based models could provide useful information. For example, consider another category of wave generation techniques without the existence of wave paddle, i.e. the internal wave maker. Based on the Boussinesq-type equations, Larsen and Dancy (1983) introduced a novel wave maker theory to generate the regular waves in shallow water condition. In their method, the free surface undulation was not induced by the wave paddle but created by using an artificial mass source term derived from the mass conservation principle. Lee and Suh (1998) developed a similar approach based on the mild slope equations and investigated the mass and energy transports of the generated wave. Furthermore, Lin and Liu (1999) proposed an internal wave generator following the mass conservation in Navier-Stokes (NS) equations and different types of the waves were generated by using this mass source function. Also, Wei et al. (1999) derived a more efficient shallow-water based transfer function that related the source amplitude to the surface wave characteristics. In their work, both the mass and momentum source functions have been presented. Later improvements have been made by Choi and Yoon (2009) and Ha et al. (2013). However, all of these investigations were based on the grid method, while there

has been no similar work carried out in the particle modeling approach so far.

In this paper, by following Wei et al. (1999) and Choi and Yoon (2009) an internal wave maker algorithm based on the momentum conservation is introduced into the ISPH method. In the formulations the momentum source term derived from the regular wave theories will be added into the NS equations as an internal particle force, which changes with the time and position. Therefore, time-dependent water waves can be easily generated through the periodic internal forces. The efficiency and accuracy of the coupled internal wave maker and ISPH model are verified by several benchmark wave simulations, including the wave generation under different wave and source region parameters, and the standing waves in front of a vertical wall. Finally, a regular wave interaction with submerged breakwater is simulated, in which the higher harmonics are separated from the main wave when it passes over the breakwater into the deep water region. This test case has been considered as being challenging for the particle-based models as it involves long time wave simulations in which the secondary wave reflection is quite substantial.

2. ISPHModel with Internal Wave Generator

2.1 Momentum source term and wave absorbing region

2.1.1 Momentum source term

In Lin and Liu's model (1999) with the mass source term, a source region was placed in the center of water flume and mass generations and deductions occurred alternately during a wave period. For the Lagrangian methods such as SPH, this mass variation process could cause the drastic increase or decrease of the particle numbers, and the numerical shocks will be inevitably induced when the particles are either added

into or removed from the computational source region. To avoid this problem, in this study the momentum source term derived by Wei et al. (1999) is added into our ISPH model as the internal wave maker instead of the mass source term. In Wei et al.'s theory, the Boussinesq equations were employed to derive the relationships between the surface elevation and the target wave. Following this, Choi and Yoon (2009) presented the general form of the momentum source function as

$$f_m(x, y, t) = \frac{1}{4\pi^2} \int_{-\infty}^{+\infty} \int_{-\infty}^{+\infty} S(x, y, \omega) \exp[i(k' y - \omega t)] dk' d\omega, \quad (1)$$

where f_m is the momentum source term with the acceleration dimension, S determines the shape of the source function, x and y denote the coordinate direction, t is the time, ω is the wave frequency and the y direction wave number is $k' = k \sin \theta$, where θ is the angle between the wave direction and x axis and k is the wave number.

The shape function S has the following form:

$$S(x, y, \omega) = D \exp(-\beta x^2), \quad (2)$$

where D is the source function amplitude and can be determined from the desired wave characteristics, and β is a parameter associated with the width of source function. D has the following form:

$$D = \frac{H_0(\omega^2 - \alpha_1 g k^4 h_0^3) \cos \theta}{\omega I_1 k [1 - \alpha (k h_0)^2]}, \quad (3)$$

where $I_1 = \sqrt{\pi / \beta} \exp[k^2 / (4\beta)]$. For the monochromatic wave, H_0 is the wave height, g is the gravitational acceleration, h_0 is the still water depth, α_1 and α are the parameters in the Boussinesq equations and they have the following relations:

$$\alpha_1 = \alpha + \frac{1}{3}, \quad (4)$$

$$\alpha = \frac{z_\alpha^2}{2h_0^2} + \frac{z_\alpha}{h_0}, \quad (5)$$

where z_α denotes the representative velocity position in a depth-averaged model, and usually takes $z_\alpha = -0.53h_0$.

The value of the source function is larger in the middle and smaller on the two sides.

Then the relationship between β and the source region width $W = 2|x_{\text{side}} - x_{\text{mid}}|$ is

$$\exp[-\beta(x_{\text{side}} - x_{\text{mid}})^2] = \exp[-\beta(\frac{W}{2})^2] \approx 0 \approx \exp(-5) \quad (6)$$

$$W = 2\sqrt{5/\beta}, \quad (7)$$

where x_{side} and x_{mid} are the positions of the lateral and middle source regions, respectively.

The relationship between the source region width W and wave length L is

$W = \delta(L/2)$, i.e. $\delta = 2W/L$, then β can be represented as

$$\beta = \frac{80}{\delta^2 L^2}, \quad (8)$$

where δ is related to the source region setup for a specific problem. As long as the source region width and wave length are known, δ is determined.

For the ISPH modeling of monochromatic waves in this study, the monochromatic wave the momentum source function vector in Eq. (1) can be simplified in the vertical

2-D form as $\tilde{\mathbf{f}}_m = (f_{mx}, f_{mz})$, where f_{mz} is zero in the present model and

$$f_{\text{mx}} = -(2g\beta x)\exp(-\beta x^2)\frac{D}{\omega}\sin(-\omega t) \quad (9)$$

This equation has the dimension of acceleration, which can be directly added into the N-S equations in the SPH methods.

2.1.2 Wave absorbing region

The proposed internal wave generator should be employed more efficiently together with a wave absorbing region to prevent the undesirable secondary wave reflections.

Following Wei and Kirby (1995), the commonly adopted absorbing coefficient has the following form:

$$A_b = c_\alpha \frac{\exp\left[\left(\frac{|x - x_{\text{st}}|}{x_{\text{ab}}}\right)^{n_c}\right] - 1}{\exp(1) - 1} \quad x_{\text{st}} < x < x_{\text{st}} + x_{\text{ab}}, \quad (10)$$

where A_b is the absorbing coefficient, x_{st} and x_{ab} are the starting position and length of the absorbing region, respectively, c_α and n_c are the empirical damping coefficients to be determined via the numerical test. Following Lin and Liu (2004), the coefficients in this model are taken as $c_\alpha = 200$ and $n_c = 10$. A_b has the unit of 1/s and will be added into the N-S equations in the next section.

As far as we know, there are not many investigations made on the wave absorbing region in particle-based methods. Xu (2010) presented a simple exponential absorbing zone to dampen the linear wave reflection, in which the absorbing length was 2 times of the wave length and the particle velocities were directly reduced at the end of each time step. Shibata et al. (2011) presented a wave absorbing method and they assigned a large viscosity value to the fluid particles in the absorbing region with a dimension of $1.98 \sim$

2.83 times of the wave length. Besides, Molteni et al. (2013) developed a matched layer approach for the shallow wave damping, in which a shorter damping distance of 1.5 wave length was used. In the present method, the absorbing length is chosen as 2.0 wave length following Wei and Kirby (1995). It is noted that equally good wave damping effects have been achieved in all of these cases.

2.2 SPH governing equations

In the ISPH method the N-S equations are written in the Lagrangian form and the advection term is automatically calculated through the tracking of particle motion. Thus the numerical diffusion arising from the successive interpolation of the advection function used in the Eulerian grid-based method is avoided in the SPH. Due to the Lagrangian nature of SPH, the internal wave generator with the mass source term is difficult to be added into the SPH equations, while for the momentum source term the adding of the additional source force could be much more straightforward. As a result, the final form of the complete mass and momentum conservation equations with the momentum source term as well as the wave absorbing term are written as

$$\nabla \cdot \bar{\mathbf{u}} = 0, \quad (11)$$

$$\frac{d\bar{\mathbf{u}}}{dt} = -\frac{1}{\rho} \nabla p + \bar{\mathbf{g}} + \nu_0 \nabla^2 \bar{\mathbf{u}} + \frac{1}{\rho} \nabla \cdot \bar{\boldsymbol{\tau}} + \bar{\mathbf{f}}_m + A_b \bar{\mathbf{u}}, \quad (12)$$

where $\bar{\mathbf{u}}$ is the particle velocity vector, ρ is the fluid density, p is the particle pressure, ν_0 is the laminar kinematic viscosity, $\bar{\boldsymbol{\tau}}$ is the sub-particle scale (SPS) turbulence stress, which was originally presented by Gotoh et al. (2001). $\bar{\mathbf{f}}_m$ is the momentum source term that changes in the x direction and keeps constant in the z direction. The detailed expression of $\bar{\mathbf{f}}_m$ has been presented in Eq. (9). A_b is the wave absorb-

ing coefficient with the expression as shown in Eq. (10).

The eddy viscosity assumption is used to model the SPS turbulence stress $\bar{\tau}$ as

$$\tau_{ij} = \rho(2\nu_t S_{ij} - \frac{2}{3}k\delta_{ij}), \quad (13)$$

where ν_t is the turbulence eddy viscosity, $S_{ij} = (\partial u_i / \partial x_j + \partial u_j / \partial x_i) / 2$ is the strain rate

k is the turbulence kinetic energy, δ_{ij} is the Kronecker delta function. The turbulence

eddy viscosity ν_t is calculated by a modified Smagorinsky model as follows:

$$\nu_t = (C_s d_0)^2 |S|, \quad (14)$$

where C_s is the Smagorinsky constant (=0.1), d_0 is the particle spacing representing

the characteristic length scale of the small eddies, and $|S| = \sqrt{|2S_{ij}S_{ij}|}$ is the local strain

rate.

In the ISPH model the two-step projection method is used to solve the N-S Eqs. (11)

and (12) which is composed of two steps. The first step is an explicit integration of ve-

locity in the time, resulting in a temporary non-zero divergence velocity field that

should be corrected in the next step. Because of the spatial variations of Eq. (9) in the x

direction, the momentum source term \bar{f}_m will generate additional divergence in the

momentum equation that needs to be corrected in the end of computational time cycle.

Similar situation also applies to the wave absorbing term $A_b \bar{u}$. Thus both of them

should be considered in the first prediction step, represented as follows without consid-

ering the pressure and gravity terms:

$$\bar{u}_* = \bar{u}_t + (\nu_0 \nabla^2 \bar{u} + \frac{1}{\rho} \nabla \cdot \bar{\tau} + \bar{f}_m + A_b \bar{u}) \Delta t, \quad (15)$$

$$\bar{r}_* = \bar{r}_t + \bar{u}_* \Delta t, \quad (16)$$

where \bar{u}_t and \bar{r}_t are the particle velocity and position at time t, \bar{u}_* and \bar{r}_* are the

temporary particle velocity and position, and Δt is the time increment.

Assuming $\Delta \bar{\mathbf{u}}_{**}$ is the changed particle velocity contributed by the remaining pressure and gravity terms, there is

$$\bar{\mathbf{u}}_{t+1} = \bar{\mathbf{u}}_* + \Delta \bar{\mathbf{u}}_{**} = \bar{\mathbf{u}}_* + \left(\bar{\mathbf{g}} - \frac{1}{\rho} \nabla p_{t+1} \right) \Delta t. \quad (17)$$

By taking Eq. (17) into the mass conservation Eq. (11), the Pressure Poisson Equation (PPE) is obtained as follows (Liu et al., 2014):

$$\nabla \cdot \left(\bar{\mathbf{g}} - \frac{1}{\rho} \nabla p_{t+1} \right) = - \frac{\nabla \cdot \bar{\mathbf{u}}_*}{\Delta t}. \quad (18)$$

The solution of PPE produces the required pressure to correct the non-zero divergence velocity fields including those contributed by the momentum source term. After obtaining the pressure field, the particle velocity is updated by Eq. (17) and the position of particle is centered in the time as

$$\bar{\mathbf{r}}_{t+1} = \bar{\mathbf{r}}_t + \left(\frac{\bar{\mathbf{u}}_t + \bar{\mathbf{u}}_{t+1}}{2} \right) \Delta t. \quad (19)$$

2.3 ISPH formulas and boundary conditions

Following Liu et al. (2014), the viscous and turbulent stress terms in Eq. (12) are given as follows:

$$(\nu_0 \nabla^2 \bar{\mathbf{u}})_i = \sum_j \left(\frac{4m_j (\mu_i + \mu_j) \bar{\mathbf{r}}_{ij} \cdot \nabla_i \mathbf{W}_{ij}}{(\rho_i + \rho_j)^2 (|\bar{\mathbf{r}}_{ij}|^2 + \eta^2)} \right) \bar{\mathbf{u}}_{ij}, \quad (20)$$

$$\left(\frac{1}{\rho} \nabla \cdot \bar{\boldsymbol{\tau}} \right)_i = \sum_j m_j \left(\frac{\bar{\boldsymbol{\tau}}_i}{\rho_i} + \frac{\bar{\boldsymbol{\tau}}_j}{\rho_j} \right) \cdot \nabla_i \mathbf{W}_{ij}, \quad (21)$$

where i and j are the reference particle and its neighbor, m is the particle mass, \mathbf{W} is the kernel function, μ is the dynamic viscosity equal to $\rho \nu_0$. $\bar{\mathbf{r}}_{ij} = \bar{\mathbf{r}}_i - \bar{\mathbf{r}}_j$,

$\bar{u}_{ij} = \bar{u}_i - \bar{u}_j$, $\nabla_i W_{ij}$ is the kernel gradient, and η is $0.1h$ to keep the denominator nonzero, where h is the smoothing length. In present 2D ISPH model, the 5th order Quintic kernel function is used.

The gravity, momentum source and wave absorbing terms are directly calculated in the arithmetic form. The pressure term is expressed as follows, as Khayyer and Gotoh (2008, 2009) have suggested:

$$\left(\frac{1}{\rho} \nabla p\right)_i = \sum_j m_j \left(\frac{p_i}{\rho_i^2} + \frac{p_j}{\rho_j^2}\right) \nabla_i W_{ij}. \quad (22)$$

Also by following Liu et al. (2014), the velocity divergence term on the right hand side of PPE Eq. (18) is discretized as

$$-(\nabla \cdot \bar{u}_*)_i = \sum_j \frac{m_j}{\rho_j} (\bar{u}_{*i} - \bar{u}_{*j}) \cdot \nabla_i W_{ij}, \quad (23)$$

and the left hand side of PPE (Eq. 18) is expressed as

$$\nabla \cdot \left(\frac{1}{\rho} \nabla p\right)_i = \sum_j \frac{8m_j}{(\rho_i + \rho_j)^2} \frac{p_{ij} \bar{r}_{ij}}{(|\bar{r}_{ij}|^2 + \eta^2)} \cdot \nabla_i W_{ij}, \quad (24)$$

where $p_{ij} = p_i - p_j$.

As for the numerical boundary conditions, the general principle is that the mirror particles are used to treat the solid boundaries and a symmetric free surface judgment criterion is used to identify the free surface particles in the ISPH computation. For further details see Liu et al. (2014) and these are not repeated here.

2.4 Implementation of internal force in source region

The detailed procedures of adding the internal force are presented in this section. The internal wave maker is located in the middle of the numerical flume with its width being smaller than a wave length. The momentum source term which is essentially an

internal force is imposed on every particle in this region. Following the Boussinesq equations, this internal force does not change in the z direction from the flume bottom to the free surface. Inside the source region, the force function has the form as shown in Eq. (9), which changes in the x direction and thus results in symmetric force pointing to both sides. The internal force is calculated by Eq. (9) with an amplitude of $-(2g\beta x)\exp(-\beta x^2)D/\omega$ and a periodic term of $\sin(-\omega t)$. The amplitude and direction of the force source term are illustrated in the black curve on top of the source region as shown in Fig. 1. The vectors in the source region denote the distributions of internal force acting on the fluid particles. The forces increase from the outside to inside areas and decrease again when approaching to the middle region ($x = 0.0$).

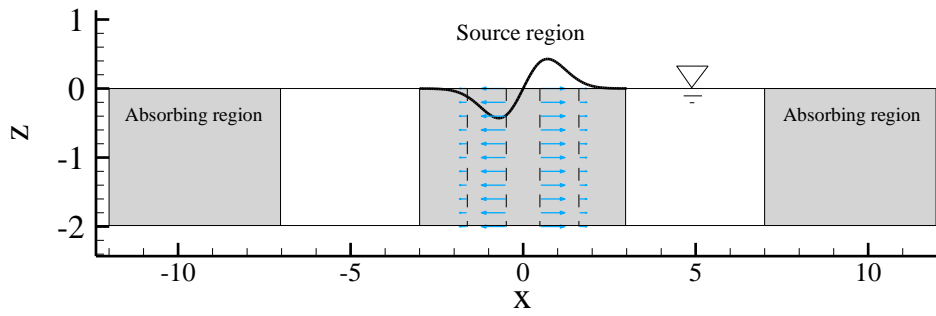


Fig. 1: The internal momentum source region.

For a still water flume without the momentum source term, a zero velocity field appears at the prediction time step, and the pressure obtained from the PPE has a hydrostatics distribution that keeps the velocity being divergence free. With the presence of momentum source term in Eq. (12), there is additional force acting on each fluid particle. During the wave generation, the internal force points to both sides to push the water out of the source region. Due to the non-uniformity of the momentum source force as shown in Fig. 1, the intermediate velocity divergence at the prediction time step is negative near the source region boundary and positive in the middle area. As a result, this

increases the pressure laterally and decreases the pressure centrally, and deviate it from the hydrostatic state. In the first half period, the free surface rises on the two sides and falls in the middle, while in the next half period, it goes the opposite way. Accordingly, a periodic wave is generated. As this force is added into the N-S equations in form of the momentum source term to generate waves, the proposed internal wave maker is not affected by the reflected waves. In this sense, the ideal non-reflection wave generation condition is achieved.

As shown in Fig. 1, the wave absorbing regions are also placed on both sides of the flume to absorb the wave near the two lateral solid boundaries. So the incident waves can be fully dissipated without any numerical shock. The above system should be able to run for quite a long time without the interference between the incident and reflected waves. It has been found that the momentum source term is very simple to implement in the SPH model so as to make it more durable for the practical purpose.

3. Model Verifications and Applications

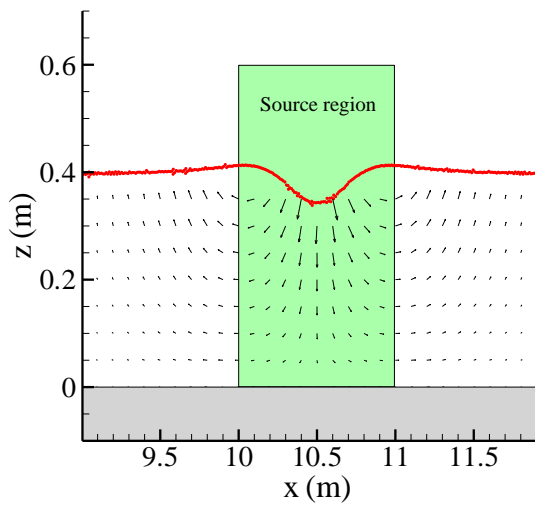
In this section, the efficiency and accuracy of the ISPH internal wave maker will be investigated through some benchmark wave simulations and wave-structure interactions.

3.1 Periodic wave generations

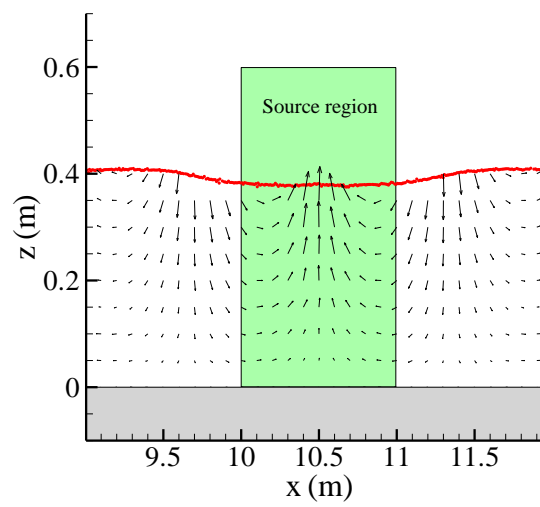
Here the proposed internal wave maker simulations will be verified by the analytical solutions of linear wave theory and the sensitivity of relevant parameters in the momentum source term will be investigated. The test problem was carried out in a numerical flume with the still water depth 0.4 m. The flume length was adjusted by following the designed wave parameters to avoid unnecessary CPU waste. The initial particle dis-

tance was 0.01 m and totally 200,000 water particles were used in the simulations. In the first case, the wave period used was 2.0 s with the internal wave generator region width being 1.0 m, which was about 25% of the wave length. The generator region was located from 10.0 m to 11.0 m (as shown in Fig. 2), within which the internal forces were added on the fluid particles. Two wave absorbing regions were placed near two sides of the flume with the length of 8.0 m, which was about twice of the wave length.

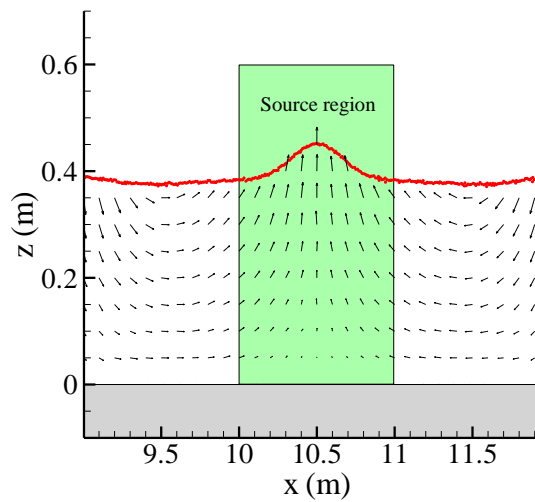
(a) $t/T = 0.25$



(b) $t/T = 0.5$



(c) $t/T = 0.75$



(d) $t/T = 1.0$

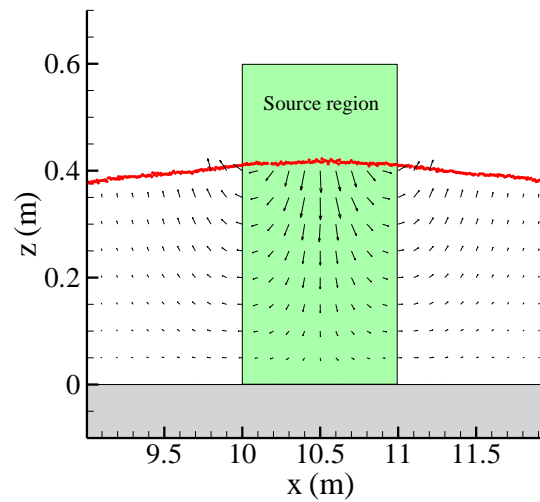


Fig. 2: Velocity field in the source region during internal wave making.

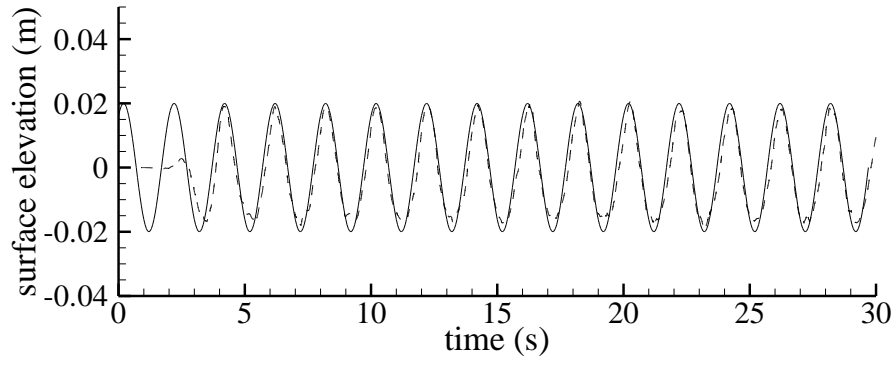
The SPH computed flow velocity fields are shown in Fig. 2 and the velocity values

were obtained through the linear interpolation of individual particle velocities for clarity. For the first half period in Fig. 2 (a), the non-zero velocity field discussed in Section 2.4 is generated from the still water and an outward velocity field is applied to the particles near the two lateral sides of the source region. Thus the water in the source region goes out and the free surface falls down to keep the velocity field divergence free. In comparison, in Fig. 2 (c), the water converges in and this results in the rising up of water surface. This alternation of increase and decrease in the water surface levels in the source region generated a continuous and stable periodic wave series. The velocity distributions in Fig. 2 demonstrated that the fluid incompressibility is largely ensured except on some individual surface particles after the correction step of ISPH projection method. It should be noted that more strict incompressibility could be achieved by using the error compensating term proposed by Khayyer and Gotoh (2011) and used by Gotoh et al. (2014) in the ISPH simulation of sloshing flows.

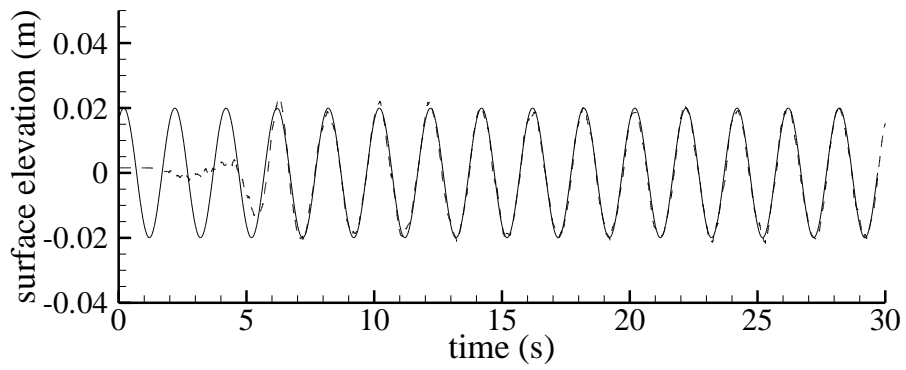
For quantitative verification, five wave gauges were placed in the flume at the position $x = 14.695$ m, 18.39 m, 22.085 m, 25.78 m and 33.17 m, with the distance from the source region being about 1.0, 2.0, 3.0, 4.0 and 6.0 times of the wavelength, respectively. The ISPH computed time histories of the water surface are illustrated in Fig. 3, compared with the analytical solutions of the linear wave theory. The numerical water surface profiles were obtained by averaging the locations of nearest four surface particles from the ISPH computation. In the simulations, a tiny phase lag was observed since the target wave was generated from a narrow region instead of a vertical line. In the comparisons, this phase lag was corrected by adjusting all of the theoretical wave phases so as to match the first wave gauge recordings. Then other simulation results could match this with one or more wave period delays according to the wave gauge position.



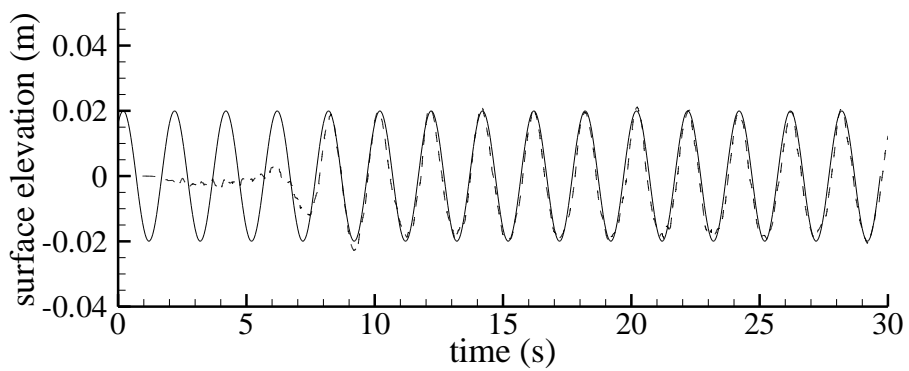
(a): $x=14.695$ m



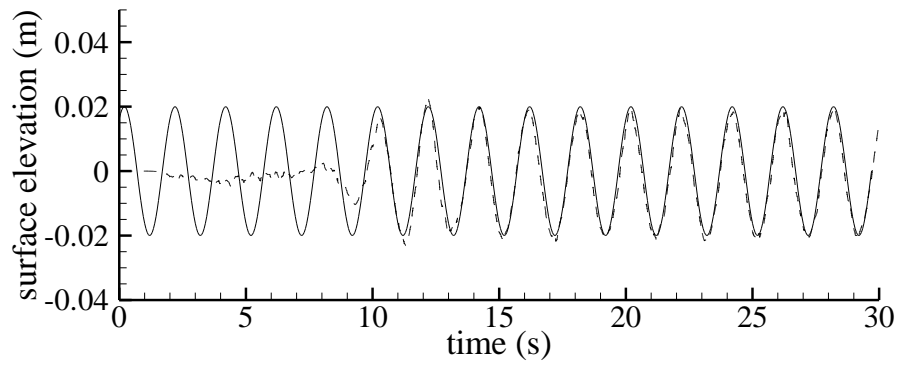
(b): $x=18.39$ m



(c): $x=22.085$ m



(d): $x=25.78$ m



(e): $x=33.17$ m

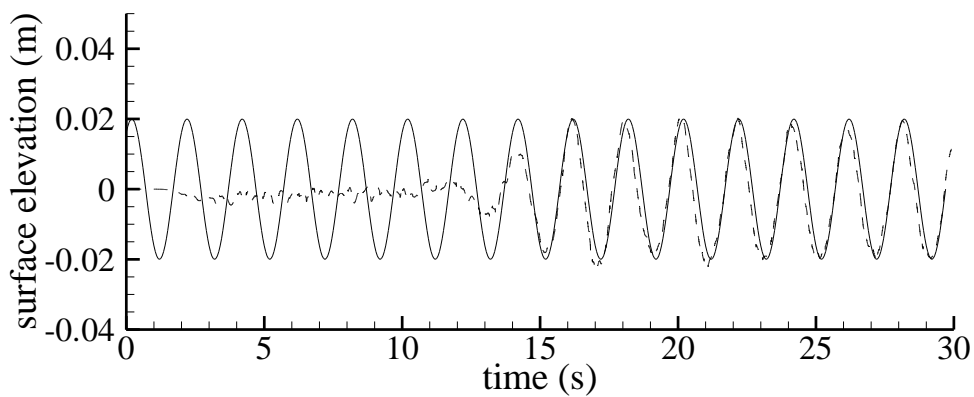


Fig. 3: Surface elevation of periodic wave generated by ISPH internal wave maker (solid line: theory, dashed line: ISPH).

In Fig. 3, it can be found that there is a flat wave trough for the result in the first gauge, which is an indication that the ISPH generated wave is still not stable. However, for the second wave gauge, the difference between the theoretical and ISPH results is relatively small. Similar phenomena are also observed on the rest three gauges, which showed that a stable wave train has been formed. The discrepancy in the first wave gauge is within expectation. As evidenced in the internal wave maker theory (Choi and Yoon, 2009), the wave parameters are usually not very accurate in the areas close to the source region. Similar issues have also been found in SPH simulations using a fixed wave paddle.

For further verification purpose, similar to the test of Choi and Yoon (2009), the

computed $u - v$ velocity profiles were presented in Fig. 4, compared with the theoretical results of linear wave theory. The measurement sections were chosen by their distances from the center of the source region at $x_{\text{mid}} = 10.5$ m and contained four nearby sections ($x' = x - x_{\text{mid}} = 0.4$ m, 1.2 m, 2.0 m and 2.8 m, i.e. $x'/h = 1.0, 3.0, 5.0, 7.0$) and two distant sections (two and three wavelengths from the source region, i.e. $x'/h = 19.725, 28.962$). From the results in Fig. 4, it is found that the discrepancies from the theoretical values are very obvious near the source region for $x'/h = 1.0$ and 3.0. However, for the other four measurement sections further away, the present internal wave maker solutions agree quite well with the linear wave theory at each x'/h .

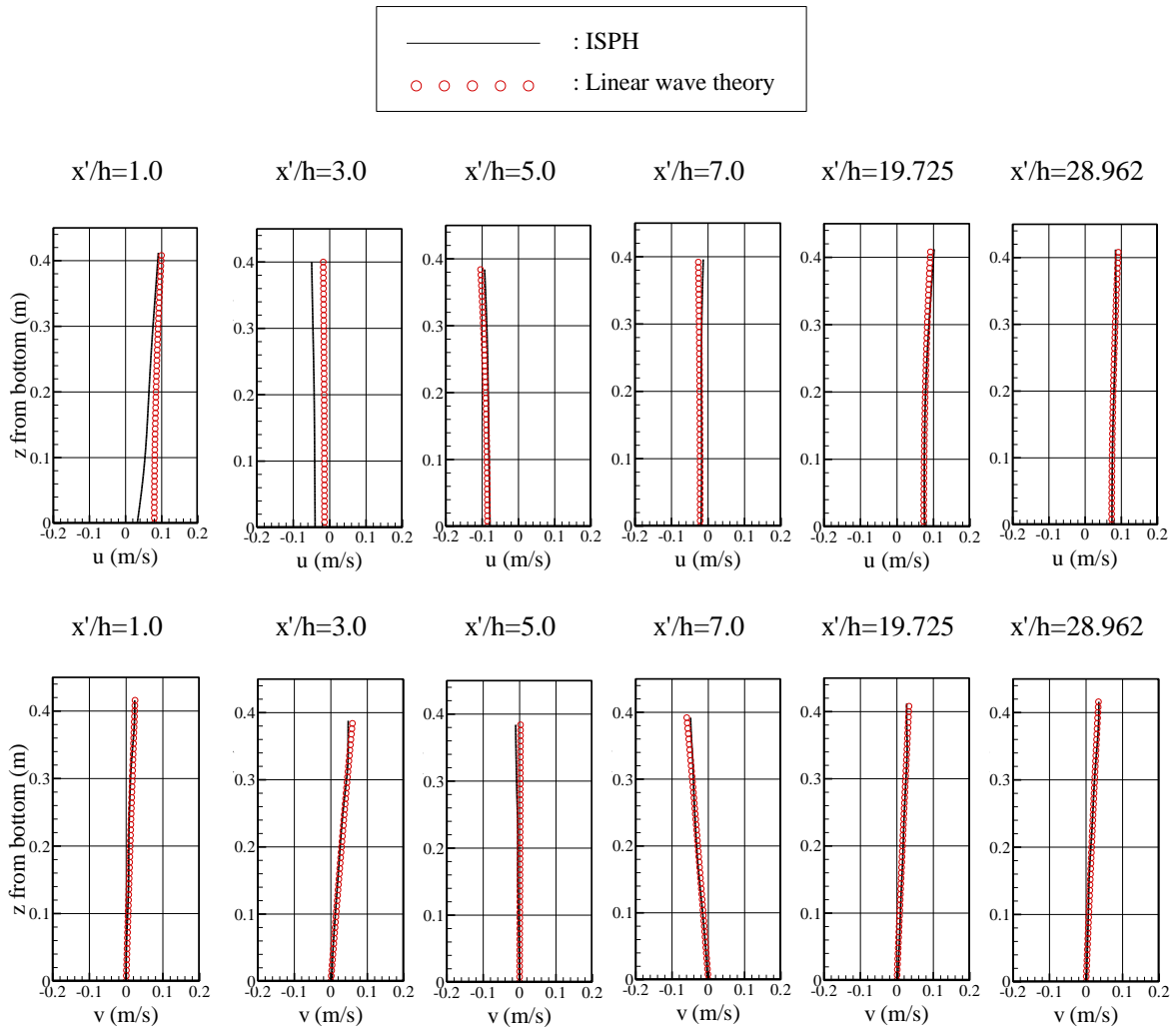


Fig. 4: Section velocity at different positions by ISPH (solid), compared with the linear wave theory (circle).

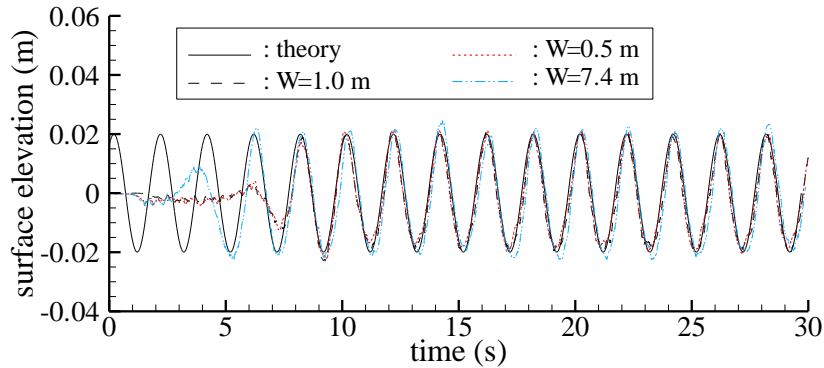
Due to the depth-averaged characteristics of the present wave maker, the evanescent wave mode could appear near the source region, but it should decay quickly away from the wave maker. This fact can be seen in the sections far away from the source region in Fig. 4, especially at $x'/h = 19.725$ and 28.962 , where the effect of evanescent wave mode was completely eliminated and the accuracy of velocity field was ensured. Similar phenomena have been found in the piston wave maker theory (Dalrymple and Dean, 1991), and also reported by Lin and Liu (1999) and Choi and Yoon (2009) in the internal wave maker theory using the grid-based models. Here it should be pointed out that in Fig. 4 the evanescent wave mode influences a range of $3h \sim 5h$, while it is $2h \sim 3h$ in Choi and Yoon (2009). The discrepancy could be attributed to the different computational conditions. Since the present ISPH wave maker employs the Boussinesq model in which the fluid parameters do not depend on the flow depth, it is not applicable for the deep water conditions. In the following section, the limitations of the method will be further investigated.

3.1.1 Sensitivity test on different source region widths

In Wei et al.'s theory (1999), there was no strict requirement on the source region width and thus the intensity distribution of input source momentum can be in any shape. In the present ISPH model, this intensity distribution is only affected by the source region width but with the total input momentum being kept constant. To test the source region effect, different region widths of $W = 0.5$ m, 1.0 m and 7.4 m (which is about 13.5%, 27% and 200% of the wavelength) are compared in the numerical simulations and the results of free surface elevations are given for the selected two gauging stations

in Fig. 5.

(a): $x=22.085$ m



(b): $x=33.17$ m

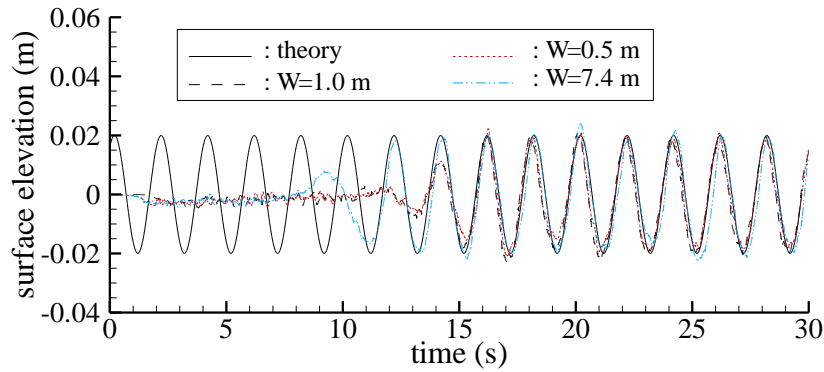


Fig. 5: Free surface elevations for different source region widths.

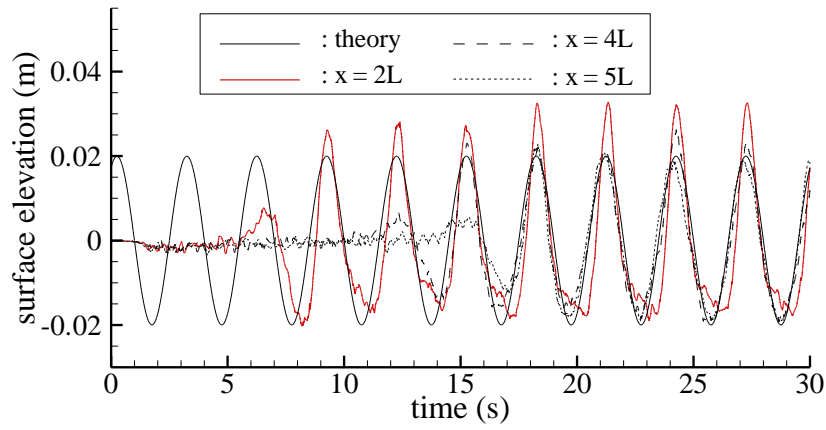
From the figure, it is seen that for the small source region width $W = 0.5$ m and 1.0 m, the target wave height and wave length are in good agreement with the linear wave theoretical values. This has indicated that the total input momentum does not change with the source region width. There is no obvious difference observed in the simulations by using either $W = 0.5$ m or 1.0 m, but a smaller source region could impose a larger momentum input on each fluid particle and result in a larger velocity and smaller time step. For example, for the case of $W = 1.0$ m, the minimum time step was about $\Delta t = 0.004$ s, while for $W = 0.5$ m the time step was reduced to $\Delta t = 0.002$ s. On the other hand, as for the results using $W = 7.4$ m in Fig. 5, the generated wave height is obvious-

ly larger than the theoretical solution. This may be due to that for the wide source region the required momentum is generated in a relatively larger space domain with more time delay, thus leading to incorrect wave parameters. By carrying out a series of additional tests, it has been found that the optimal source region width is about 20% ~ 50% of the wave length in this study, by balancing both the target wave accuracy and the computational efficiency.

3.1.2 Sensitivity test on different wave lengths

Relatively accurate results have been obtained for the above case with $T = 2.0$ s that represents the medium length wave. In this section, the sensitivity tests of numerical result on different wave lengths will be studied. Similar setup as employed in the previous section is used, except that two different wave periods $T = 0.7$ s and 3.0 s are considered, which represent the short and relatively long waves. In order to eliminate the influence of source region width on the computational results, the region width is fixed as 0.228 m and 1.73 m for these two additional runs, respectively. Also, it has been checked that this dimension falls within the optimal source region range (30% of wavelength) as mentioned before, thus the interpretation of numerical results can objectively disclose the wave length effects. Several wave gauges were placed at different locations using the multiples of the wave length to measure the free surface elevations, and the results are presented in Fig. 6.

(a) $T = 3.0$ s



(b) $T = 0.7$ s

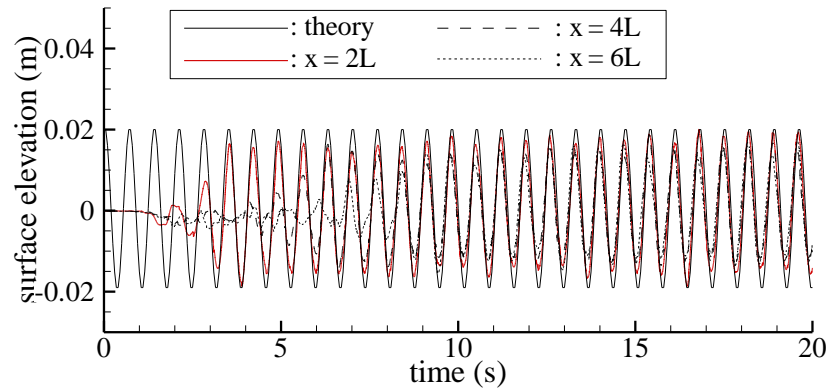


Fig. 6: Free surface elevations for different wave periods (wave lengths).

From the figure, it is found that for the long wave generation ($T = 3.0$ s), the surface elevation on the wave gauge at $x = 2L$ is much higher than the theoretical value. At $x = 4L$ and $5L$, the generated wave profiles approach to the theoretical solutions and also become stable. The reason can be explained as follows. In the wave propagation region within $x = 4L$, the source region velocity field needs time to gradually adjust to the real target wave velocity field. For the long wave generation in a constant water depth, larger input momentum is generated than that under the short wave condition, so the adjustment distance becomes relatively longer as a result. In comparison, for the short wave with $T = 0.7$ s, the generated waves can become stable very quickly within $2L$ distance but the mean wave height is much smaller than the target wave height. The sit-

uation becomes worse further away from the source region. This may be due to that the present internal wave maker theory is based on the Boussinesq equations so all of the flow variables are assumed to be depth-averaged. For the short wave in a real water flume, since the velocity near the free surface is always larger than that near the flume bottom, the accuracy of wave generation theory based on the depth-averaging concept deteriorates. In the following case studies, we will focus on the long wave simulations, although further work on the short waves should also be carried out in details.

3.2 Wave reflection from a vertical wall

In this part, the ISPH internal wave maker model will be applied to the problem of wave reflections from a vertical wall. In this simulation, the periodic waves are generated in the middle of the flume and then propagate to both lateral directions. The still water depth is 0.5 m and initial particle distance is 0.01 m. The source region is from $x = 10.0$ m to $x = 11.0$ m, and the wave damping zone is placed on the left side of the flume from $x = 0.0$ m to $x = 6.0$ m. The right side of flume is a solid vertical wall to fully reflect the incident waves. If there is no interaction between the reflected wave and the momentum source region and also the wave damping zone can absorb the wave series as efficiently as like a single wave train, we may expect the following scenarios: the total internal reflection will only happen on the right wall and a standing wave should be generated between the source region and the right wall. Besides, in the region between the source region and the damping zone, a wave group composed of two monochromatic wave trains, should propagate in the same direction with the same wave height and frequency but in a different phase.

As shown in Fig. 7, the black points represent the free surface particle trajectories from 45 s to 50 s when the stable waveform has been formed. The wave form on the

right (standing wave) and left (propagating wave) sides of the source region can be expressed by using the linear wave theory as

$$\eta_{\text{right}} = \eta_i + \eta_r = \frac{H_0}{2} \cos(kx - \omega t) + \frac{H_0}{2} \cos(kx + \omega t) = H_0 \cos(kx) \cos(\omega t) \quad (25)$$

$$\eta_{\text{left}} = \frac{H_0}{2} \cos(kx - \omega t) + \frac{H_0}{2} \cos(kx - \omega t - \phi) \quad (26)$$

where η_{right} and η_{left} are the wave surface elevations in two different regions, respectively. η_i and η_r represent the incident and reflected wave profiles, and ϕ is the phase difference between two waves in the left region. In this case, the phase difference can be obtained by assuming that the wave is generated in the middle of source region at $x = 10.5$ m. So the reflected wave arrives at the middle line after propagating a distance of $2 \times (30.0 - 10.5) = 39.0$ m, which contains 9.614 wavelengths, i.e. 9.614 period lags. Based on this, the theoretical results of surface profile (envelope lines) in the standing wave region (right) and propagating wave region (left) can be obtained and employed to verify the ISPH simulation results. The envelope lines are shown in Fig. 7 in the form of dashed and solid lines, respectively, for the two different regions.

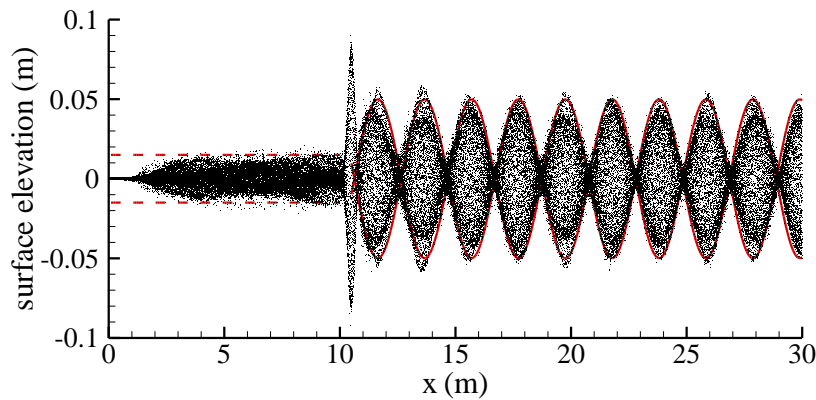


Fig. 7: ISPH computed wave reflections from a vertical wall, and solid and dashed lines represent theoretical surface envelopes in two wave regions.

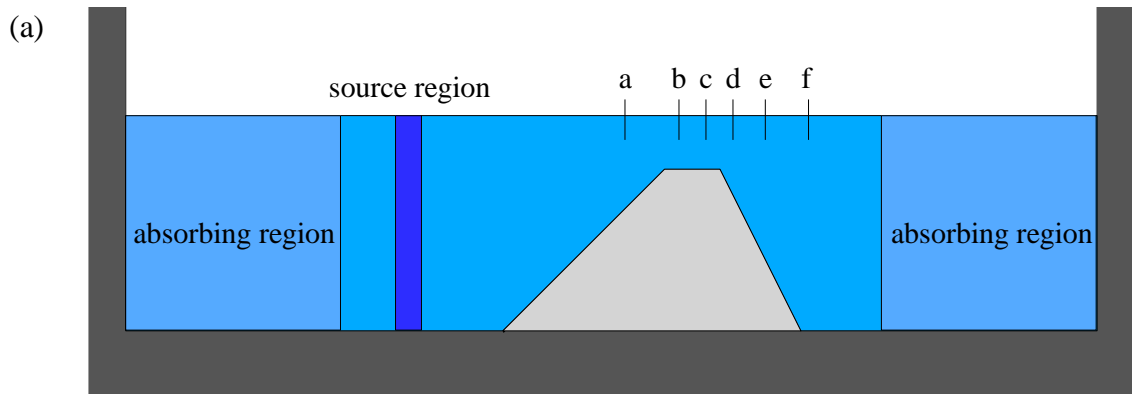
From the figure, it is found that in the area between the source region and right wall, very good agreement between the theoretical values and ISPH simulation results has been achieved, with the exception of a very few number of individual particles being outside of the envelope line. Besides, in the area on the left side of source region, equally good agreement is found outside the damping region from $x = 6.0$ m to $x = 10.0$ m. The efficiency of wave absorbing layer is also demonstrated by the fact that the wave height decreases to nearly zero in front of the left wall due to the wave damping effect. The above comparisons showed that the present internal wave maker has an influence on the reflected waves passing through the momentum source region. Here it is worth mentioning that the present internal wave maker may not give more accurate results than the traditional wave making methods by using a numerical wave paddle. However, by using the momentum source term, satisfactory non-reflection wave generation technique can be achieved for the ISPH model which enables longer time wave simulations.

3.3 Wave decomposition on a trapezoid breakwater

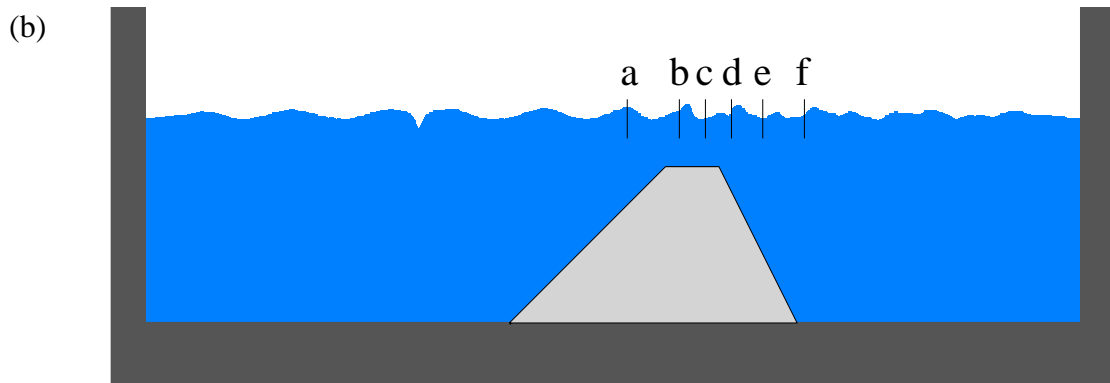
There are many trapezoid breakwaters in the ocean engineering field, which maintain a steady water surface for the port or other coastal structures. The interaction between the wave and breakwater is also a popular topic among the SPH researchers ([Rogers et al., 2010](#); [Suwa et al., 2013](#); [Altomare et al., 2014](#); [Ren et al., 2014](#)). Harmonic generation or decomposition occurs above the breakwater and this phenomenon results in the energy being transferred from the first harmonic to the higher bound harmonics of the incident wave ([Mei and Ünlüata, 1972](#)). On re-entering the deeper water on the downstream side of the breakwater, these higher harmonics are released as the free waves. This has a significant impact on the transmitted wave energy, which cannot be simply predicted by the linear wave theory. With an increase in the steepness of the

incident wave, this highly nonlinear phenomenon can become more significant (Christou et al., 2008).

In this section, the experimental data of Beji and Battjes (1993) is used to validate the present ISPH model with the proposed internal wave maker. The wave decomposition case is generally used as the critical test for a numerical wave model due to the complicated wave-wave and wave-structure interactions.



The problem setup



snapshots at $t = 43.0$ by present model

Fig. 8: Wave decomposition on a trapezoid breakwater.

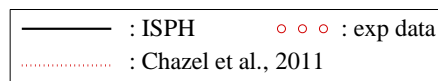
The numerical setup of the problem is shown in Fig. 8 (a) by following the experiment of Beji and Battjes (1993). The bottom of the 2-D numerical flume is horizontal with a total length of 36 m. The momentum internal wave maker is located in the region from $x = 10.0$ m to 11.0 m and the wave absorbing region is placed on both sides of the

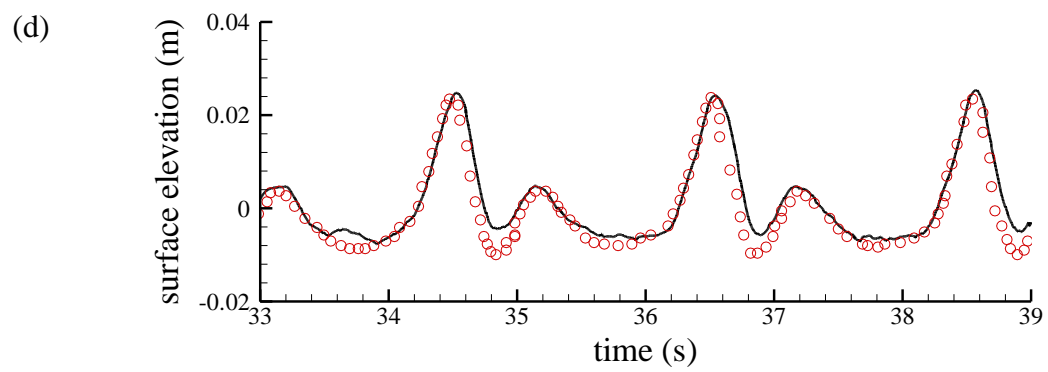
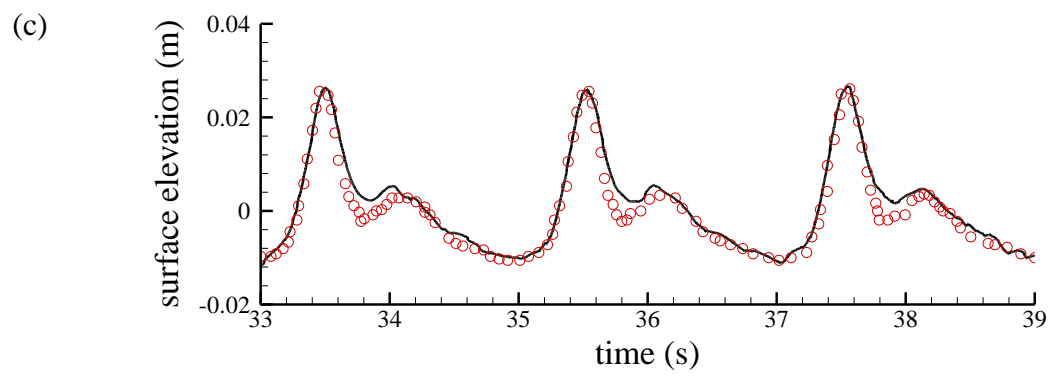
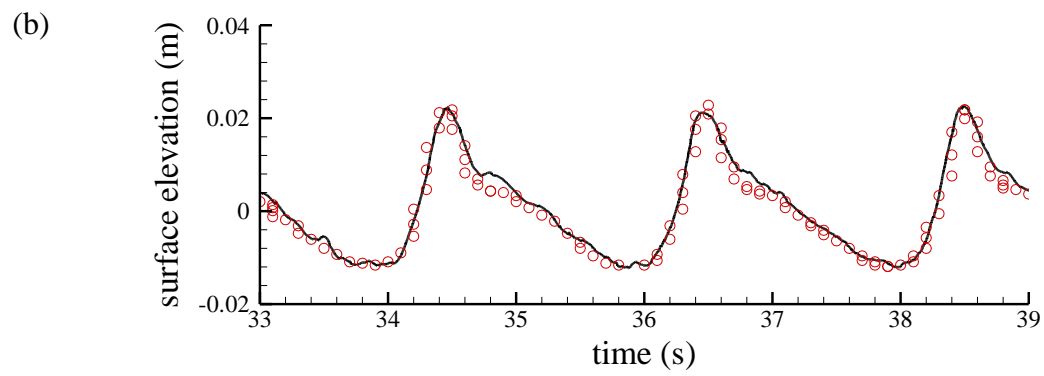
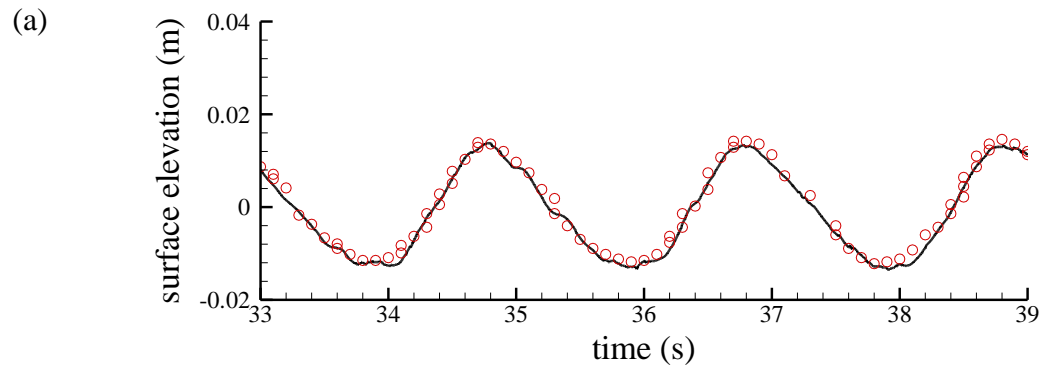
flume with the length of 8.0 m. The transmitted and reflected waves are absorbed by these damping regions so the whole simulation can run for a long time without the influence of the secondary reflection. The trapezoid breakwater is located in the region from $x = 14.0$ m to 25.0 m with a front slope 1/20 and a back slope 1/10. The water depth on the top of breakwater is 0.1 m and the still deep water depth in the flume is 0.4 m. Six wave gauges (a) - (f) were used in the experiment at $x = 18.5$ m, 20.5 m, 21.5 m, 22.5 m, 23.7 m and 25.3 m to measure the free surface elevations. In the ISPH simulations, the initial particle distance is $d_0 = 0.005$ m and totally 520,000 (half million) fluid particles are employed. The incident wave period is 2.02 s and the wave height is 0.02 m.

Prior to the numerical simulation of wave-structure interaction, we removed the breakwater and tested the wave generation and propagation on a flat bottom. The ISPH computed wave surface elevations at the six wave gauges were observed to be very close to the theory values from the linear wave theory, which proved the accuracy of the model under specified wave conditions. The formal simulations were then carried out up to 50 seconds although the stable waveforms had been developed at all wave gauges after 10.0 s. The target wave was generated in the source region and it propagated towards the breakwater. The waveform in this region is the direct superposition of the incident and reflected waves as shown in Fig. 8 (b), which also shows the wave decomposition snapshots on the onshore side of the breakwater.

The ISPH computed wave surface profiles at six wave gauges are compared with the experimental data of Beji and Battjes (1993) in Fig. 9 (a) - (f). When the main wave begin to climb the slope, the wave height increases slightly as shown in Fig. 9 (a) due to the effect of wave shoaling. Also a slight increase of the wave steepness is observed in

Fig. 9 (a) - (b) for the same reason. At the wave gauge (c) on the top of the breakwater, the high-order harmonic wave begins to develop and a secondary wave appears. During this process, the wave energy is redistributed and part of it is taken away by the harmonic waves with a different phase velocity, as shown in Fig. 9 (c) - (d). Behind the breakwater, the secondary wave mode gains more energy from the main wave and the harmonic effect becomes stronger, which can be seen at the wave gauge (e). The prediction of wave transformation in the region where wave gauges (e) and (f) are located is the most difficult one because of the complicated flow separations and nonlinear wave energy transfers. Generally speaking, the comparisons between the ISPH simulations and experimental results of Beji and Battjes (1993) are quite good in the first two gauges (a) - (b), while there exist some kind of differences in the wave trough for the other four gauges (c) - (f). The overall good agreement with the experimental data on the surface elevations at all wave gauges is an indication that the proposed non-reflection wave generation process by using the internal wave maker works quite well for the ISPH model. To further evaluate the ISPH model performance, the numerical results of Chazel et al. (2011) by using a grid model are also shown in Fig. 9 (e) and (f) for a comparison. It is shown that the ISPH results agree better with the experimental wave crests while the Chazel et al.'s (2011) results agree better with the experimental wave troughs, and two numerical models can equally predict the wave decomposition and deformation processes in a satisfactory manner.





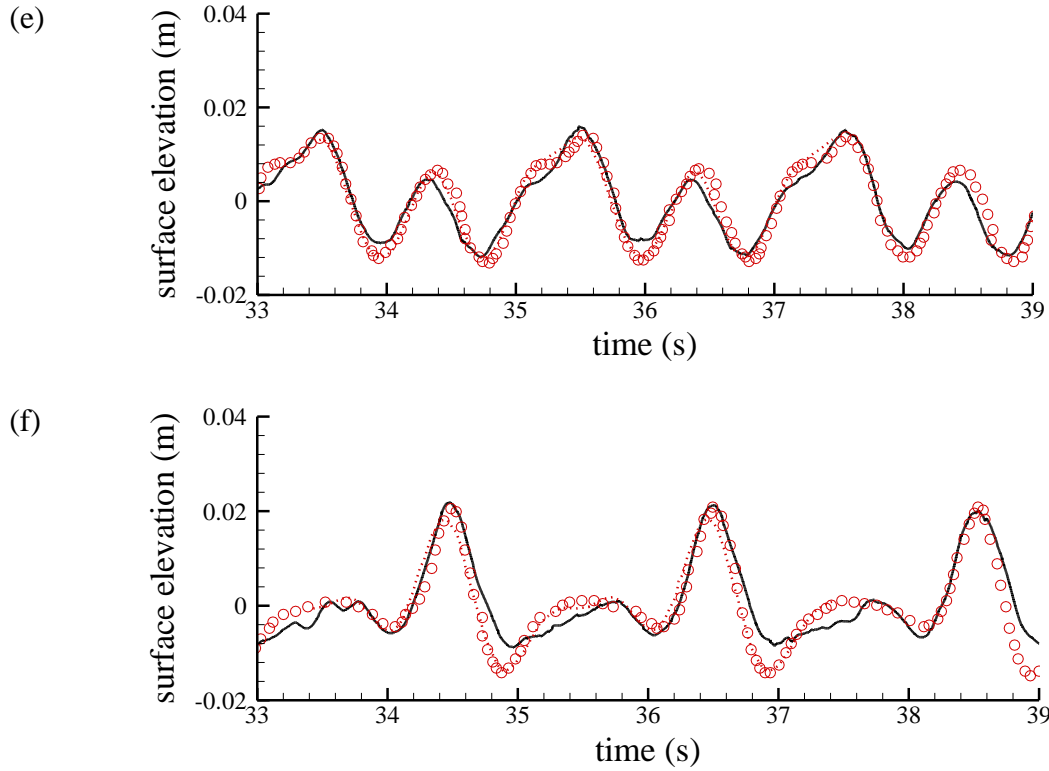


Fig. 9: Free surface elevations on six wave gauges (a) - (f), computed by ISPH internal wave maker model, compared with experimental data (Beji and Battjes, 1993) and grid based method (Chazel et al., 2011, at e and f).

To demonstrate the stability of the computational waveforms, the long time simulation results are presented in Fig. 10, in which the recorded data are taken from 10 s to 45 s for the selected wave gauges (b), (d) and (e) (marked with b, d and e in Fig. 10). It should be noted that the experimental data are only presented for 3 wave periods for a comparison. In theory, without the use of the internal wave maker and the wave absorbing region, the secondary reflection waves will reach the breakwater after about 28.0 s and then lead to unrealistic wave deformations. In the figure, due to the use of the internal wave maker, the stable waveforms can be observed from 10.0 s to 45.0 s in that both the wave shapes and wave amplitudes are almost the same during this time. This has proved that the secondary reflection wave is nearly eliminated and the ISPH model

can run for any arbitrarily longer time depending on the simulation interest.

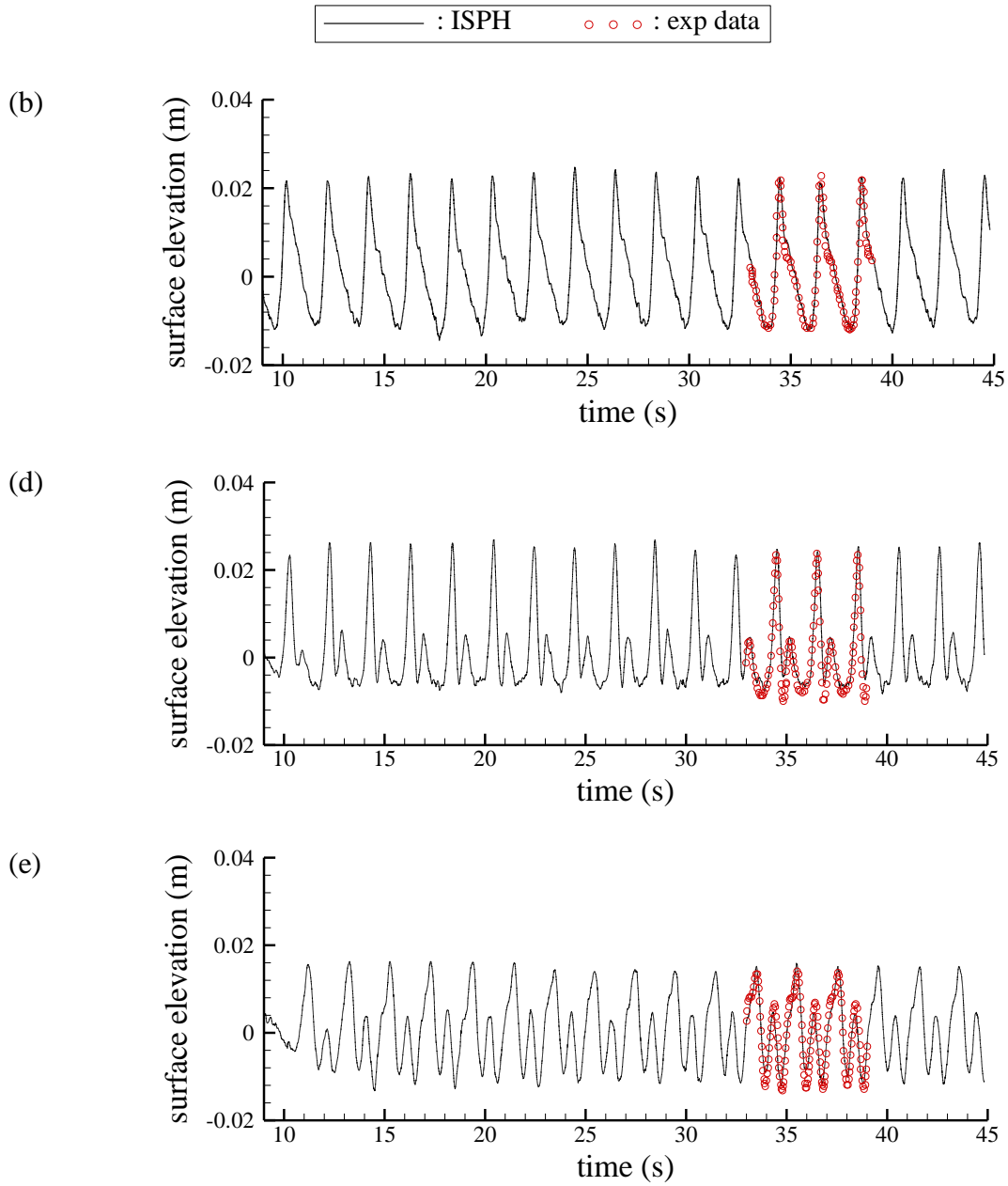


Fig. 10: Long time ISPH simulations of wave surface profiles using internal wave maker at wave gauges (b), (d) and (e), compared with experimental data of Beji and Battjes (1993).

4. Conclusion

In this paper, the non-reflection wave maker theory originated from the mesh-based

method is introduced into the mesh-free ISPH model. The proposed internal wave maker algorithm employs an internal force to generate the periodic waves using a momentum source term and thus does not cause the secondary wave reflection which is inevitable when a solid numerical wave paddle is used. The internal force equation is derived from the Boussinesq equations based on the momentum conservation, which is straightforward to implement in the ISPH algorithms.

Through a series of sensitivity tests on the propagating wave, it has been found that the present ISPH wave maker model is more efficient under the relatively medium and long wavelength conditions and the optimal momentum source region width is 20% ~ 50% of the wavelength. Furthermore, the wave reflection from a vertical wall has been simulated and a stable standing wave train is formed with the computed wave surface profiles being consistent with the theoretical envelop lines. In the last case, 520,000 particles are employed for the simulations of wave decomposition on a trapezoid breakwater. The ISPH computations have been carried out for a long time and quite stable wave profiles have been obtained, which shows that the secondary wave reflection effect is eliminated and the accuracy of internal wave maker model is satisfactory for the non-reflection wave generation. In conclusion, the proposed internal wave maker algorithm provides an alternative way to study the long-time wave propagations and wave-structure interactions using the particle-based method.

However, it should be realized that the present model can only generate linear waves in a vertical 2-D domain. Future work needs to be carried out to develop the depth-resolved momentum source function so that some nonlinear waves, such as the higher-order Stokes wave, can be generated by the ISPH internal wave maker model. Besides, 3D wave generation should also be possible based on the present internal wave

maker algorithm as long as a 3D ISPH solver is available.

5. Acknowledgement

This research work is supported, in part, by the National Key Basic Research Program of China (2013CB036401), China Postdoctoral Science Foundation (2014M552358), National Natural Science Foundation of China (NSFC 51279120; 51479126, 51479087).

References

- Altomare, C., Crespo, A.J.C., Rogers, B.D., Dominguez, J.M., Gironella, X., Gómez-Gesteira, M., 2014. Numerical modelling of armour block sea breakwater with smoothed particle hydrodynamics. *Comput. Struct.* 130, 34-45.
- Beji, S., Battjes, J.A., 1993. Experimental investigation of wave propagation over a bar. *Coastal Eng.* 19, 151-162.
- Chazel, F., Lannes, D., Marche, F., 2011. Numerical simulation of strongly nonlinear and dispersive waves using a Green-Naghdi model. *J. Sci. Comput.* 48(1-3), 105-116.
- Choi, J., Yoon, S.B., 2009. Numerical simulations using momentum source wave-maker applied to RANS equation model. *Coastal Eng.* 56, 1043-1060.
- Christou, M., Swan, C., Gudmestad, O.T., 2008. The interaction of surface water waves with submerged breakwaters. *Coastal Eng.* 55, 945-958.
- Dalrymple, R.A., Dean, R.G., 1991. *Water Wave Mechanics for Engineers and Scientists*. Prentice-Hall.
- Dao, M.H., Xu, H., Chan, E.S., Tkalich, P., 2013. Modelling of tsunami-like wave

- run-up, breaking and impact on a vertical wall by SPH method. *Nat. Hazards Earth Syst. Sci.* 13, 3457-3467.
- Didier, E., Neves, M.G., 2012. A semi-infinite numerical wave flume using smoothed particle hydrodynamics. *Int. J. Offshore Polar Eng.* 22(3), 193-199.
- Du, X., Wu, W., Gong, K., Liu, H., 2006. Two dimensional SPH simulation of water waves generated by underwater landslide. *J. Hydrodyn. Ser. A* 21(5), 579-586 (in Chinese).
- Frigaard, P., Brorsen, M., 1995. A time domain method for separating incident and reflected irregular waves. *Coastal Eng.* 24, 205-215.
- Gallati, M., Braschi, G., Falappi, S., 2005. SPH simulations of the waves produced by a falling mass into a reservoir. *Nuovo Cimento C Geophys. Space Phys. C* 28, 129.
- Gotoh, H., Sakai, T., 1999. Lagrangian simulation of breaking waves using particle method. *Coastal Eng. J.* 41(3&4), 303-326.
- Gotoh, H., Shibahara, T., Sakai, T., 2001. Sub-particle-scale turbulence model for the MPS method - Lagrangian flow model for hydraulic engineering. *Comput. Fluid Dyn. J.* 9, 339-347.
- Gotoh, H., Khayyer, A., Ikari, H., Arikawa, T., Shimosako, K., 2014. On enhancement of Incompressible SPH method for simulation of violent sloshing flows. *Appl. Ocean Res.* 46, 104-115.
- Ha, T., Lin, P.Z., Cho, Y.S., 2013. Generation of 3D regular and irregular waves using Navier–Stokes equations model with an internal wave maker. *Coastal Eng.* 76, 55-67.
- Hayashi, M., Gotoh, H., Memita, T., Sakai, T., 2000. Gridless numerical analysis of wave breaking and overtopping at upright seawall. *Proc. ICCE* 3, 2100-2113.

- Khayyer, A., Gotoh, H., 2008. Development of CMPS method for accurate water-surface tracking in breaking waves. *Coastal Eng. J.* 50(2), 179-207.
- Khayyer, A., Gotoh, H., 2009. Modified Moving Particle Semi-implicit methods for the prediction of 2D wave impact pressure. *Coastal Eng.* 56(4), 419-440.
- Khayyer, A., Gotoh, H., 2011. Enhancement of stability and accuracy of the moving particle semi-implicit method. *J. Comput. Phys.* 230(8), 3093-3118.
- Koshizuka, S., Nobe, A., Oka, Y., 1998. Numerical analysis of breaking waves using the moving particle semi-implicit method. *Int. J. Numer. Methods Fluids* 26(7), 751-769.
- Larsen, J., Dancy, H., 1983. Open boundaries in short wave simulations - a new approach. *Coastal Eng.* 7, 285-297.
- Lee, C., Suh, K.D., 1998. Internal generation of waves for time-dependent mild slope equations. *Coastal Eng.* 34, 35-57.
- Lin, P., Liu, P.L.F., 1999. Internal wave-maker for Navier-Stokes equations models. *J. Waterw. Port Coastal Ocean Eng.* 125(4), 207-215.
- Lin, P., Liu, P.L.F., 2004. Discussion of vertical variation of the flow across the surf zone. *Coastal Eng.* 50, 161-164.
- Liu, X., Lin, P.Z., Shao, S.D., 2014. An ISPH simulation of coupled structure interaction with free surface flows. *J. Fluids Struct.* 48, 46-61.
- Mei, C.C., Ünlüata, U., 1972. Harmonic generation in shallow water waves. In: Meyer, R.E. (Ed.), *Waves on Beaches and Resulting Sediment Transport*. Academic Press, pp. 181-202.
- Molteni, D., Grammauta, R., Vitanza, E., 2013. Simple absorbing layer conditions for shallow wave simulations with Smoothed Particle Hydrodynamics. *Ocean Eng.* 62,

78-90.

- Monaghan, J.J., 1994. Simulating free surface flow with SPH. *J. Comput. Phys.* 110, 399-406.
- Ren, B., Wen, H., Dong, P., Wang, Y., 2014. Numerical simulation of wave interaction with porous structures using an improved smoothed particle hydrodynamic method. *Coastal Eng.* 88, 88-100.
- Rogers, B.D., Dalrymple, R.A., Stansby, P.K., 2010. Simulation of caisson breakwater movement using 2-D SPH. *J. Hydraul. Res.* 48(S1), 135-141.
- Shibata, K., Koshizuka, S., Sakai, M., Tanizawa, K., 2011. Transparent boundary condition for simulating nonlinear water waves by a particle method. *Ocean Eng.* 38(16), 1839-1848.
- Skillen, A., Lind, S., Stansby, P.K., Rogers, B.D., 2013. Incompressible smoothed particle hydrodynamics (SPH) with reduced temporal noise and generalised Fickian smoothing applied to body-water slam and efficient wave-body interaction. *Comput. Meth. Appl. Mech. Eng.* 265, 163-173.
- Suwa, T., Nakagawa, T., Murakami, K., 2013. A study of the wave transformation passing over an artificial reef using SPH method. *J. Comput. Sci. Technol.* 7(2), 126-133.
- Wei, G., Kirby, J.T., 1995. Time-dependent numerical code for extended Boussinesq equations. *J. Waterw. Port Coastal Ocean Eng.* 121, 251-261.
- Wei, G., Kirby, J.T., Sinha, A., 1999. Generation of waves in Boussinesq models using a source function method. *Coastal Eng.* 36(4), 271-299.
- Xu, R., 2010. An Improved Incompressible Smoothed Particle Hydrodynamics Method and Its Application in Free-surface Simulations. PhD Dissertation, University of

Manchester, UK. http://wiki.manchester.ac.uk/spheric/index.php/SPH_PhDs.

Zheng, J.H., Soe, M.M., Zhang, C., Hsu, T.W., 2010. Numerical wave flume with improved smoothed particle hydrodynamics. *J. Hydrodyn. Ser. B* 22(6), 773-781.